



Beyond sixfold coordinated Si in SiO₂ glass at ultrahigh pressures

Clemens Prescher^{a,b,1}, Vitali B. Prakapenka^b, Johannes Stefanski^a, Sandro Jahn^a, Lawrie B. Skinner^{c,d}, and Yanbin Wang^b

^aInstitut für Geologie und Mineralogie, Universität zu Köln, 50674 Köln, Germany; ^bCenter for Advanced Radiation Sources, University of Chicago, Chicago, IL 60637; ^cX-Ray Science Division, Advanced Photon Source, Argonne National Laboratory, Argonne, IL 60439; and ^dMineral Physics Institute, Stony Brook University, Stony Brook, NY 11794-2100

Edited by Russell J. Hemley, The George Washington University, Washington, DC, and approved August 1, 2017 (received for review May 30, 2017)

We investigated the structure of SiO₂ glass up to 172 GPa using high-energy X-ray diffraction. The combination of a multichannel collimator with diamond anvil cells enabled the measurement of structural changes in silica glass with total X-ray diffraction to previously unachievable pressures. We show that SiO₂ first undergoes a change in Si–O coordination number from fourfold to sixfold between 15 and 50 GPa, in agreement with previous investigations. Above 50 GPa, the estimated coordination number continuously increases from 6 to 6.8 at 172 GPa. Si–O bond length shows first an increase due to the fourfold to sixfold coordination change and then a smaller linear decrease up to 172 GPa. We reconcile the changes in relation to the oxygen-packing fraction, showing that oxygen packing decreases at ultrahigh pressures to accommodate the higher than sixfold Si–O coordination. These results give experimental insight into the structural changes of silicate glasses as analogue materials for silicate melts at ultrahigh pressures.

high pressure | polymorphism | glass | oxygen packing

The structure of silicate melts and glasses at high pressure is of great interest not only in physics, geophysics, and materials science, but also in engineering and industry. Their physical properties at high pressures and temperatures have fundamental influences on present-day magmatic processes and the evolution of the early Earth (1, 2). Seismological heterogeneities at the top of the transition zone (3, 4) and at the core–mantle boundary (5) have been interpreted with the potential presence of silicate melts at very high pressures in the Earth's interior. At ambient conditions, polymerized silicate melts and glasses are characterized mainly by networks of Si–O tetrahedra (6). Experimental investigations (7–10) and molecular dynamics (MD) simulations (11, 12) have shown that Si–O coordination number (CN) increases from fourfold to sixfold between 15 and 40 GPa, resulting in a network of Si–O octahedra (13). At pressures >40 GPa, MD simulations indicate a continuous increase in Si–O CN in SiO₂ glass (11) and SiO₂ melt (12), whereas existing experimental data on SiO₂ glass indicate a plateau of sixfold coordinated Si–O up to 100 GPa from total X-ray diffraction analysis (9) and up to 140 GPa inferred from shear soundwave velocities (14).

A recent compilation of glass and melt structure data (15) found that evolution of network-forming structural motifs can be rationalized in terms of oxygen-packing fraction (OPF). A plateau region for fourfold coordinated A atoms (A = Si, Ge, Al, etc.) is found for an OPF of 0.4–0.6. The transformation to sixfold coordination occurs rapidly as OPF approaches 0.64. The highest experimental CN measured for SiO₂ so far is 6 at 100 GPa (9), indicating another plateau for sixfold CN. However, recent data for GeO₂ glass, which serves as a structural analogue for SiO₂ glass, show a CN larger than sixfold, up to 7.4 at 92 GPa (16). These data follow the trend seen from MD simulations, where it has been shown that CN continuously increases with pressure after the relatively sharp fourfold to sixfold transition has taken place.

We have conducted measurements of the SiO₂ glass structure factors up to 172 GPa using angular dispersive X-ray diffraction using a combination of diamond anvil cells (DACs) with a multichannel collimator (MCC) (17). The MCC, which was originally developed for Paris–Edinburgh Presses, effectively reduces the background scattering of the surrounding DAC, thus enabling total X-ray diffraction up to very high pressures and extending the pressure range for total X-ray diffraction with an angle dispersive setup by more than a factor of 3 (previously 50–60 GPa; e.g., ref. 7) for relatively low Z elements.

Selected structure factors $S(Q)$ and pair distribution functions $g(r)$ of the SiO₂ glass up to 172 GPa are shown in Fig. 1. The $S(Q)$ shows strong changes up to 33 GPa, whereby the main feature is a peak rising between 2 and 3 Å⁻¹ and a decrease in the intensity of the first sharp diffraction peak (FSDP). From 33 to 172 GPa, the $S(Q)$ changes very smoothly with no apparent new features.

Figs. 2–4 show the pressure dependence of the FSDP position and the Si–O CN and Si–O distances, respectively. The FSDP position increases almost linearly with pressure up to ~20 GPa, followed by a gradual curvature to another linear regime with a much smaller slope from 50 to 172 GPa. Our FSDP positions are in good agreement with refs. 8, 9, and 18, whereas refs. 7 and 19 reported slightly lower values at >25 GPa. The data used in refs. 19 and 9 are the same, and the discrepancy can probably be explained by different methods for extracting FSDP positions. The large change in FSDP positions at low pressures can be associated with a strong change in intermediate-range order. The accompanied drop in intensity also indicates a large decrease in void space in the structure (20) and ring closure (21), which is

Significance

The combination of multichannel collimator and diamond anvil cells enabled the investigation of the real-space structure of an amorphous material >100 GPa. We have measured the structure of SiO₂ glass by angle-dispersive X-ray diffraction up to 172 GPa. Our results are in agreement with existing data up to 50 GPa showing a sharp change from fourfold to sixfold Si–O coordination number (CN). However, at higher pressures, CN continuously increases to values beyond 6 without sharp structural changes. The behavior of SiO₂ glass at high pressure serves as a model for more complex silicate glasses and melts. Thus, our results provide experimental insight into the structural evolution of silicate glasses and melts at ultrahigh pressures.

Author contributions: C.P., V.B.P., and Y.W. designed research; C.P. and V.B.P. performed the experiments; C.P., V.B.P., and L.B.S. analyzed the data; J.S. and S.J. performed and analyzed the simulations; and C.P. wrote the paper with contributions from all other authors.

The authors declare no conflict of interest.

This article is a PNAS Direct Submission.

¹To whom correspondence should be addressed. Email: clemens.prescher@gmail.com.

This article contains supporting information online at www.pnas.org/lookup/suppl/doi:10.1073/pnas.1708882114/-DCSupplemental.

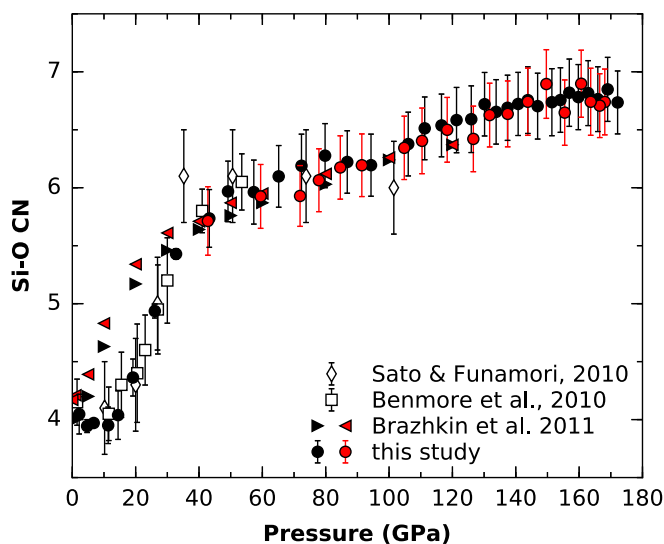


Fig. 3. Pressure dependence of Si–O CN in SiO₂ glass in comparison with previous experimental data (7, 9) and MD simulations (11). Black and red symbols represent compression and decompression, respectively.

be different degrees of anhydrostaticity. Sato et al. (24) have shown that differential stress results in large differential strain in SiO₂ glass <20 GPa, whereas the strain decreases with higher pressures.

Our data show that the structure of SiO₂ continuously changes with pressure from 50 up to 172 GPa. We do not see evidence for a stable plateau with a CN of 6 at higher pressures as reported for SiO₂ glass (9) and GeO₂ glass (16), but, rather, a continuous increase in CN up to ~ 7 at 172 GPa. Furthermore, we do not observe first-order structural changes at 140 GPa, as predicted from soundwave velocity measurements of SiO₂ glass (14). If existent, the origin of those sound speed changes might lie in other mechanisms or be caused by the different experimental approaches. For example, it might be specific to the laser interaction with the glass and the very long collection time needed for a Brillouin spectroscopy measurement >140 GPa, resulting in possible structural changes and/or densification.

In comparison with the glass at high pressure, crystalline SiO₂ undergoes a succession of phase transformations with increasing pressure, depending on the state of the starting material (25). Experimental investigations have shown that, for example, α -quartz transforms to coesite at ~ 2.5 GPa, to a rutile-type structure (stishovite) at ~ 10 GPa, to a CaCl₂-type structure at ~ 60 GPa, to α -PbO₂ structure (seifertite) at 120 GPa, and a polymorph with $Pa\bar{3}$ space group >270 GPa, which has been suggested to be a pyrite like structure due to the same space group (26). Many of those phase transformations are not readily occurring at room temperature and need heating at the relevant pressures to overcome kinetic barriers. Room temperature compression of different SiO₂ starting materials has been shown to lead to a variety of other metastable polymorphs (25, 27) or even amorphization at high pressures (28). Beyond current experimental achievable pressure, a cotunnite SiO₂ structure has been predicted at >750 GPa (29). However, a later detailed search for different structure types at ultra-high pressures has found the Fe₂P-type structure to be more stable than the cotunnite structure (30). This structure type was predicted to be stable at >650 GPa. Lyle et al. (31) further predicted an $I4/mmm$ structure at >10 TPa. It is remarkable that in almost all of those high-pressure structure types, except for the predicted structures >650 GPa, the first-neighbor maximum Si–O CN is 6. Only in the very high-pressure struc-

tures, Si was either 9-fold coordinated in the cotunnite-type and Fe₂P-type structures or 10-fold coordinated in the $I4/mmm$ structure. The steady increase of the Si–O CN with pressure >50 GPa in the glass observed here suggests that amorphous and crystalline SiO₂ exhibit different densification mechanisms at very high pressures.

However, a closer look at the second Si–O neighbor distances in crystalline SiO₂ shows a decrease with each subsequent structural transformation. While it was 2.952 Å for CaCl₂-type structure at 70 GPa, it was only 2.372 Å for the suggested pyrite structure of the $Pa\bar{3}$ -type polymorph at 270 GPa. In fact, the pyrite type structure can be either described as 6- or 8-coordinated Si with six small and two longer Si–O bonds. Thus, it is reasonable that the randomly distorted structure of the SiO₂ glass could reach higher Si–O CN than 6 at high pressures. If we assume linear increase of the CN with pressure, extrapolation of the Si–O CN to higher pressures reaches a value of 8 at ~ 325 GPa, which is only slightly higher in pressure than the observed transition to the pyrite structure in crystalline SiO₂ at 270 GPa (26).

The changes of CN with pressure in oxide glasses and oxide melts have been shown to be linked to the OPF (15). Due to the lack of glass and melt structural data with a CN >6, the systematics in Zeidler et al. (15) is reported only for CNs between 3 and 6. Kono et al. (16) reported the first data on above-sixfold Ge–O CN in GeO₂ glass at high pressures. They extended the systematics by using a similar approach to calculate OPF for structures with above sixfold CN. The OPF η_0 is calculated by $\eta_0 = V_O \rho c_O$, with $V_O = (4/3)\pi r_O^3$, where r_O is the oxygen radius, c_O is the atomic fraction of oxygen, and ρ is number density. The number densities were taken from density measurements of the respective glasses at high pressures or by extrapolation of this data by using different equation of state (EOS) formalisms, when experimental density data are not available. The oxygen radii are more difficult to obtain, since the apparent O–O peaks in experimentally derived $g(r)$ do not necessarily represent the shortest O–O distance. For example, by comparing the distances of the apparent O–O peak of the SiO₂ glass at high pressures to the distances in crystalline analogue structures, it is clear that there has to be contributions with lower O–O distance than the peak position suggests. This can also be seen, for example, by the height increase of the minimum between the Si–O peak and the neighboring O–O peak in the $g(r)$ with

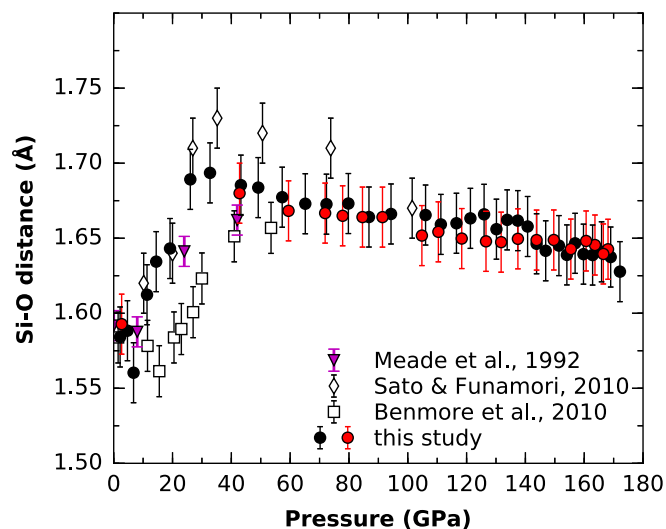


Fig. 4. Pressure dependence of the Si–O bond distance in SiO₂ glass. Values are compared with previous X-ray diffraction data (7–9). Black and red symbols represent compression and decompression, respectively.

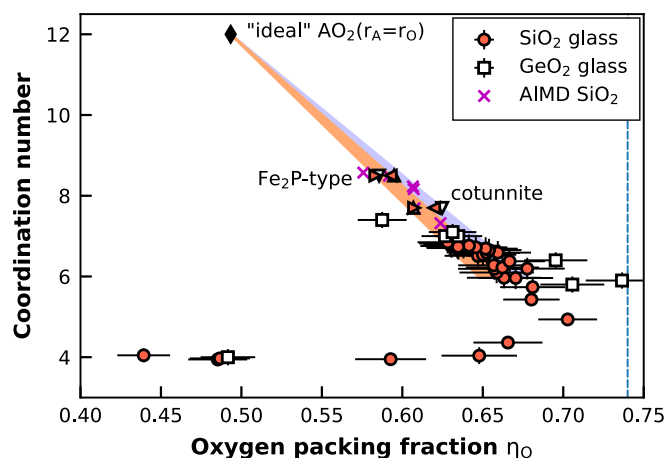


Fig. 5. Dependence of OPF on A–O CN for SiO₂ glass from this study and GeO₂ glass from ref. 16. We compare experimental data to calculated values for the Fe₂P-type and cotunnite structural polymorphs for SiO₂ (red left/right triangles) (30) and GeO₂ (white up/down triangles) (32). Hereby, different directions of the symbols are for different cutoff values (2.1 and 2.5 Å) for the O–O MEFIR distance calculations for these crystal structures. The dashed blue line represents the Kepler conjecture (KC) marking the densest possible OPF [~ 0.74 (34)]. The black diamond represents an “ideal” hypothetical close-packed AO₂ structure where both atoms have the same size and contribute to the close packing equally; thus, A–B coordination will be 12, but the OPF η_N is only two-thirds of the KC. The shaded areas are linear extrapolations from the ideal AO₂ structure through the values of predicted crystalline high pressure phases to sixfold coordination. The magenta crosses show the results of the ab initio MD (AIMD) simulation for different densities (7–16 g/cm³ at 4,000 K).

pressure (Fig. 1B). In Zeidler et al. (15), the A–O distance is used as reference distance, and the O–O distance is calculated from geometric considerations (e.g., $r_O = r_{Ge-O}/\sqrt{2}$ for sixfold coordination in octahedral geometry). There, O–O distances for structures with a CN between 3–4 and 4–6 are calculated as weighted averages from the corresponding polyhedra, assuming a linear dependence. Kono et al. (16) applied this principle for sixfold to ninefold CN by using the GeO₂ cotunnite-type structure predicted by first-principles calculations (32). They calculated the r_O/r_{Ge-O} ratio using average Ge–O and O–O distances up to 2.54 Å in the predicted cotunnite structure and applied this ratio for estimating the oxygen radius in the glass.

However, the atomic radii should be more closely represented by the smallest distances, whereas the larger distances are often induced by the specific medium-range structure of the material. To correct for this effect and obtain a more robust estimate, we used a different approach. We calculated the oxygen radius in the predicted ultrahigh pressure structures using the concept of mean fictive ionic radii (MEFIR) (33), which weighs shorter bond distances more than larger bond distances. On this basis, we recalculated $r_O/r_{Ge-O} = 0.593$ and $r_O/r_{Si-O} = 0.59$ for the predicted cotunnite structure of GeO₂ and SiO₂, respectively. For the predicted GeO₂ and SiO₂ Fe₂P-type structures, we obtained $r_O/r_{Ge-O} = 0.576$ and $r_O/r_{Si-O} = 0.575$, respectively. Furthermore, while the apparent Ge–O/Si–O CN for both structures, cotunnite-type and Fe₂P-type, is 9, the polyhedron of the cotunnite-type structure is much more distorted. To account for this distortion, Hoppe (33) introduced the concept of effective CN (ECoN), which counts the contribution from atoms deviating from the closest distance slightly less. This results in an ECoN of 7.7 for the cotunnite structure and of 8.5 for Fe₂P-type structure. Using these values, we have calculated the OPF–CN systematics for our SiO₂ glass data and recalculated the systematics for the GeO₂ glass data (16).

For the SiO₂ glass data, we used the Fe₂P-type structure as endmember, and for the GeO₂ glass data, we used the cotunnite structure as endmember, since these have been predicted to be the next stable crystalline phases at pressures higher than the maximum pressure reached in each experimental study, respectively (30, 32). The results are shown in Fig. 5.

The η_O –CN systematics of SiO₂ glass up to sixfold coordination followed the trend in the compilation of ref. 15. The OPF η_O for fourfold Si–O coordination ranged from 0.44 to 0.67. At this η_O , the Si–O CN increased to ~ 6 . Above sixfold Si–O CN, η_O actually decreased, rather than remaining more or less constant, as reported for GeO₂ (16). However, this is an expected behavior: A close-packed oxygen structure only has fourfold (tetrahedral) and sixfold (octahedral) gaps; thus, to increase the Si–O CN to a larger value, the structure has to depart from a closed packed oxygen arrangement. The increasing CN > 6 is caused by the increasing ionic radius ratio r_{Si}/r_O at very high pressures (Fig. S1). This results in an increasing Si-packing fraction by the expense of the OPF, while the total packing η_{total} of the glass structure remains more or less constant (Fig. S2). If we imagine a closed packed structure of an ideal AO₂ compound with $r_A = r_O$, where both atoms are building the packing structure, η_O would be 0.49 (2/3 of the KC). Projecting from this ideal AO₂ structure through the SiO₂ and GeO₂ Fe₂P-type and cotunnite-type structure points in the η_O –CN plot explains the behavior of the SiO₂ glass with CN between 6 and 7 very well, as shown in Fig. 5. Those results do not necessarily imply that the structure of the SiO₂ glass will eventually reach a η_{total} of the KC at 0.74. It could also be that η_{total} maximum remains at ~ 0.71 up to ultrahigh pressures, as is approximately seen for our high-pressure SiO₂ glass data in Fig. S2. However, the projection in Fig. 5 clearly shows the trend that Si plays a more and more important role in building the packing structure of the SiO₂ glass at ultrahigh pressures, which will inevitably also result in larger and larger CNs. Another important point to make here is that η_O and η_{total} of the SiO₂ glass at pressures > 20 GPa are already above the so-called optimal random close packing (RCP) limit of equal spheres [~ 0.64 (Fig. S2)] (35). This implies that this optimal RCP limit, which was empirically derived for hard sphere objects, does not necessarily apply for glass structures.

The recalculated Ge–O CN to oxygen packing systematics of GeO₂ glass data from Kono et al. (16) shows a similar trend as seen for the SiO₂ glass (Fig. 5). Whereas the calculations in Kono et al. (16) give a constant oxygen packing > 6 CN (see figure 6 in ref. 16), using the MEFIR estimation of the oxygen radius in combination with the lower ECoN number of the cotunnite structure results in a decreasing η_O for CNs > 6 . This is following the predicted trend extrapolated from the ideal AO₂ to the predicted Fe₂P-type cotunnite structures. Thus, the decreasing OPF, and therefore a deviation from a closed packed oxygen lattice for CNs > 6 , seems to be a general behavior of crystalline and amorphous AO₂ structures.

To test our method of using MEFIR and ECoN of the predicted high-pressure structures as a basis for extrapolation above sixfold Si–O coordination, we performed ab initio MD (AIMD) simulations of SiO₂ glass at very high densities, from 7 to 16 g/cm³. The simulations were done at 4,000 K to have enough kinetic energy for the structures to relax in a reasonable time frame and reach pseudostable configurations, but not enough temperature to be in the molten state for these densities. While the AIMD simulations might not be a perfectly accurate description of how the SiO₂ glass would behave at those very high densities due to the limited simulation time and small number of atoms, it still is a viable tool for predicting the general behavior of SiO₂ at ultrahigh pressures. The AIMD simulation η_O –CN results plot remarkably well in the predicted region spanned between the extrapolated ideal AO₂ structure and the

predicted high-pressure polymorphs (Fig. 5), thus, confirming the validity of our approach for the calculation of η_{O-CN} systematics for the SiO_2 and GeO_2 glasses for above sixfold Si-O coordination.

Materials and Methods

Experimental Details. The high-pressure X-ray diffraction experiments were performed at the GSECARS, 13-IDB beamline, Advanced Photon Source, Argonne National Laboratory. A BX90 DAC (36) was used for pressure generation, and all measurements were collected at room temperature. An incident monochromatic X-ray beam with an energy of 40 keV and $2.5 \times 3 \mu\text{m}$ beam size was used. An MCC as described in ref. 17 with a $50\text{-}\mu\text{m}$ inner slit size and $200\text{-}\mu\text{m}$ outer slit size was used. Commercially available SiO_2 glass was packed in the pressure chamber in a Re gasket; beveled diamonds with $120\text{-}\mu\text{m}$ culet size were used; and no pressure medium was used. A small piece of gold was added as pressure calibrant, whereby pressure was estimated before and after each measurement based on the known equation of state (EOS) of gold (37), with the reported pressures being the average, and the difference was used as error estimate. Diffraction data were collected with a Mar345 image plate detector, which was calibrated by using a LaB_6 standard. The typical collection time was 300 s.

Data Analysis. Detector calibration, image integration, and intensity corrections for oblique X-ray to detector angle, c-BN seat and diamond absorption were performed by using the Dioptas software package (38). The resulting diffraction patterns were corrected for an additional diamond Compton scattering contribution, which was necessary because the background measurement before compression was measured with a thicker sample chamber than the compressed sample material at high pressure (Fig. S3). The thinner sample chamber resulted in more diamond in the volume of diffraction constrained by the MCC. Both the sample signal and the additional diamond Compton scattering contribution were corrected for the transfer function of the MCC (39).

The Faber-Ziman structure factors and pair distribution functions were calculated by using the Glassure software package (40). The data-processing steps included: (i) normalization to atomic units by fitting the high part of the wave vector Q to the calculated scattering factors of SiO_2 , (ii) extrapolation of the resulting $S(Q)$ to zero by using a second-order polynomial function with $y = a(x^2 - c) + b(x - c)$, with $y = 0$ for $x < c$, and (iii) optimization of the data using a Kaplow-type correction (41) with typically three iterations. The amount of extra diamond Compton scattering n_{dia} was optimized by minimization of the amplitude of the oscillations before the first peak in $g(r)$ after Fourier transformation from $S(Q)$ to $g(r)$ before any Kaplow-type correction (41). The resulting n_{dia} are shown in Fig. S4. No Lorch-modification (42) function was used, since it was found to be unnecessary. Number densities for calculation of $g(r)$ and CNs were estimated by using two third-order Birch-Murnaghan EOSs for different pressure regions: (i) up to 45 GPa with $\rho_0 = 2.212 \text{ g/cm}^3$, $K_0 = 18.88 \text{ GPa}$ and $K' = 3.53$; (ii) $>45 \text{ GPa}$ with $\rho_0 = 3.86 \text{ g/cm}^3$, $K_0 = 176 \text{ GPa}$ and $K' = 4.5$.^{*} These EOSs have been determined by X-ray absorption up to almost 100 GPa. Because our data did not show any sign of abrupt structural changes $>100 \text{ GPa}$, we assumed the estimated EOS parameters to be valid up to 172 GPa. Example analyses at 5 GPa and 172 GPa are shown in Figs. S5 and Fig. S6, respectively.

CN Estimation. In principle CNs can be extracted from the calculated pair distribution functions $g(r)$ by integrating over the first peak. This works directly for monatomic materials. However, for materials with two or more elements, there exists no direct solution, since $g(r)$ is influenced by weighing of the partial $S(Q)$ with the X-ray form factors $f(Q)$ for each element. One way to overcome this is by calculating pseudopartial structure factors through reweighing of the original $S(Q)$ using the X-ray form factors $f(Q)$ for Si and O:

$$wf(Q) = \frac{(c_{Si}f_{Si} + c_{O}f_{O})^2}{2c_{O}c_{Si}f_{O}(Q)f_{Si}(Q)}$$

$$S_{Si-O}(Q) = (S(Q) - 1) \cdot wf + 1$$

where $wf(Q)$ is the weighing factor, c_O and c_{Si} are the relative concentrations of each element ($c_O = 2/3$ and $c_{Si} = 1/3$), $f_O(Q)$ and $f_{Si}(Q)$ are the X-ray form factors for Si and O, respectively. By performing the Fourier trans-

form of $S_{Si-O}(Q)$, we obtain the pseudopartial pair distribution function $g_{Si-O}(r)$:

$$g_{Si-O}(r) = wf(0) - 1 + \frac{1}{2\pi^2\rho r} \int_0^{Q_{max}} Q[S_{Si-O}(Q) - 1] \sin(Qr)dQ$$

where ρ is the number density in atoms per cubic Å (e.g., 0.0662 \AA^{-3} for SiO_2 glass at ambient conditions). This partial pair distribution function can now be used to estimate the Si-O CN by integrating over the first peak, provided that the peak is only from an Si-O contribution. In this case, we do an integration over the full peak up to the first minimum in the $4\pi\rho r^2g(r)$ curve after the peak:

$$CN_{Si-O} = 4\pi\rho c_O \int_0^{r_{min}} r^2 g_{Si-O}(r) dr. \quad [1]$$

However, this method is only reliable if the peak is well separated and we are sure there is no other contribution (e.g., from O-O). In the case for the SiO_2 glass data at high pressures, this method works very well up to sixfold coordination at $\sim 40\text{--}50 \text{ GPa}$. At higher pressures, it is known from crystalline polymorphs of SiO_2 that the O-O distances can be as low as 1.9 \AA ,—for example, for $\alpha\text{-PbO}_2$ type SiO_2 at $\sim 120 \text{ GPa}$ using the EOS data of ref. 51, which will be well within the integration area (the usual r_{min} is at $\sim 2.1 \text{ \AA}$) and thus leading to erroneously high Si-O CNs. To avoid this issue, we can also assume that the peak is symmetric and integrate over the left half of the peak and double the intensity, whereby the r_{max} will be the maximum in $r^2g(r)$ of the first peak:

$$CN_{Si-O} = 8\pi\rho c_O \int_0^{r_{max}} r^2 g_{Si-O}(r) dr. \quad [2]$$

This maximum peak integration method is only reliable if the distribution is symmetric, which is often not the case for glasses. Depending on the type of asymmetry of the peak, the different methods will give upper and lower limits of the actual average CN present in the glass. For the analysis of the SiO_2 glass presented here, we chose to use Eq. 1 for the CN up to 40 GPa, because the peak is well separated, and we can account for the asymmetric peak shape. Eq. 2 was used at higher pressures to avoid the artificially high CN due to the extra O-O contribution. Comparison between the extracted CN of both methods is shown in Fig. S7. The minimum method [Eq. 1] leads to very high CNs $> 30 \text{ GPa}$, probably due to extra O-O contributions, and the peak maximum method leads to slightly higher CNs $< 30 \text{ GPa}$, due to not representing the slight asymmetric nature of the Si-O peak and therefore overestimating the CN. The CN errors were calculated by the variation within the estimate of the r -space uncertainty used for the Si-O distances.

Computational Details. The AIMD simulations are based on a PBE exchange correlation functional (43) in conjunction with Goedecker-type (44) pseudopotentials as implemented in the CPMD code (45). Born-Oppenheimer simulations were performed in canonical ensemble with a Nosé-Hoover thermostat (46, 47) and with 264 atoms. An integration time step of 0.3 fs was used, and each density was equilibrated for at least 3 ps. Parameters from the simulations were extracted from a subsequent production run with a run time of at least 6 ps. A good compromise between accuracy and computation speed was found for the plane-wave expansion of the Kohn-Sham orbitals with a cutoff of 100 Ry. We calculated η_O based on box size and number of O atoms in the simulation cell and the Si-O CN was estimated by integrating the first peak of the time averaged Si-O pair distribution function up to the first minimum after the peak (Eq. 1).

The starting configuration for the AIMD simulations was produced by classical MD (CMD) simulations using the DL-POLY Classic code (48) in combination with Morse potentials (49, 50) and a time step of 1 fs. The CMD simulations were run in the NPT ensemble with a Nosé-Hoover thermostat (46, 47). An initial randomized cell was created with 264 atoms and a number density of $0.066 \text{ atoms/\AA}^3$, whereby atoms were moved until all atomic distances were above reasonable cutoff distances ($d_{Si-O} > 1.4 \text{ \AA}$; $d_{O-O} > 2 \text{ \AA}$ and $d_{Si-Si} > 2 \text{ \AA}$). This cell was then equilibrated at ambient pressure and 3,000 K for 100 ps. After this, the cell was equilibrated at 70 GPa and 5,000 K for 1,000 ps. This structure produced by the CMD simulations was further equilibrated by an AIMD run of $>30 \text{ ps}$ at 4,000 K.

ACKNOWLEDGMENTS. We thank S. Petitgirard for providing preliminary EOS data for SiO_2 glass. Y.W. was supported by NSF Grant EAR-1620548. Portions of this work were performed at GeoSoilEnviroCARS (The University

^{*}Petitgirard S, et al. (2017) Goldschmidt Conference, August 13–18, 2017, Paris.

of Chicago, Sector 13), Advanced Photon Source (APS), Argonne National Laboratory. GeoSoilEnviroCARS is supported by NSF Earth Sciences Grant EAR-1128799 and Department of Energy (DOE) GeoSciences Grant DE-FG02-94ER14466. This research used resources of the APS, a DOE Office of Science User Facility operated for the DOE Office of Science by Argonne National Laboratory under Contract DE-AC02-06CH11357. We thank the Gauss Center for Supercomputing (GCS) for providing computing time for a GCS Large

Scale Project on the GCS share of the supercomputer JUQUEEN (51) at Jülich Supercomputing Center (JSC). GCS is the alliance of the three national supercomputing centers, Höchstleistungsrechenzentrum Stuttgart (Universität Stuttgart), JSC (Forschungszentrum Jülich), and Leibniz-Rechenzentrum (Bayerische Akademie der Wissenschaften), funded by the German Federal Ministry of Education and Research and the German State Ministries for Research of Baden-Württemberg, Bayern, and Nordrhein-Westfalen.

1. Stixrude L, de Koker N, Sun N, Mookherjee M, Karki BB (2009) Thermodynamics of silicate liquids in the deep Earth. *Earth Planet Sci Lett* 278:226–232.
2. Tonks WB, Melosh HJ (1993) Magma ocean formation due to giant impacts. *J Geophys Res* 98:5319–5333.
3. Revenaugh J, Sipkin SA (1994) Seismic evidence for silicate melt atop the 410-km mantle discontinuity. *Nature* 369:474–476.
4. Song TRA, Helmberger DV, Grand SP (2004) Low-velocity zone atop the 410-km seismic discontinuity in the northwestern United States. *Nature* 427:530–533.
5. Williams Q, Garnero EJ (1996) Seismic evidence for partial melt at the base of Earth's mantle. *Science* 273:1528–1530.
6. Wright AC (1994) Neutron scattering from vitreous silica. V. The structure of vitreous silica: What have we learned from 60 years of diffraction studies? *J Non Cryst Sol* 179:84–115.
7. Benmore CJ, et al. (2010) Structural and topological changes in silica glass at pressure. *Phys Rev B* 81:054105.
8. Meade C, Hemley RJ, Mao HK (1992) High-pressure x-ray diffraction of SiO₂ glass. *Phys Rev Lett* 69:1387–1391.
9. Sato T, Funamori N (2010) High-pressure structural transformation of SiO₂ glass up to 100 GPa. *Phys Rev B* 82:184102.
10. Sato T, Funamori N (2008) Sixfold-coordinated amorphous polymorph of SiO₂ under high pressure. *Phys Rev Lett* 101:255502.
11. Brazhkin VV, Lyapin AG, Trachenko K (2011) Atomistic modeling of multiple amorphous-amorphous transitions in SiO₂ and GeO₂ glasses at megabar pressures. *Phys Rev B* 83:132103.
12. Karki BB, Bhattarai D, Stixrude L (2007) First-principles simulations of liquid silica: Structural and dynamical behavior at high pressure. *Phys Rev B* 76:104205.
13. Teter DM, Hemley RJ, Kresse G, Hafner J (1998) High pressure polymorphism in silica. *Phys Rev Lett* 80:2145–2148.
14. Murakami M, Bass JD (2010) Spectroscopic evidence for ultrahigh-pressure polymorphism in SiO₂ glass. *Phys Rev Lett* 104:025504.
15. Zeidler A, Salmon PS, Skinner LB (2014) Packing and the structural transformations in liquid and amorphous oxides from ambient to extreme conditions. *Proc Natl Acad Sci USA* 111:10045–10048.
16. Kono Y, et al. (2016) Ultrahigh-pressure polyamorphism in GeO₂ glass with coordination number >6. *Proc Natl Acad Sci USA* 113:3436–3441.
17. Mezouar M, et al. (2002) Multichannel collimator for structural investigation of liquids and amorphous materials at high pressures and temperatures. *Rev Sci Instrum* 73:3570–3574.
18. Inamura Y, Katayama Y, Utsumi W, Funakoshi KI (2004) Transformations in the intermediate-range structure of SiO₂ glass under high pressure and temperature. *Phys Rev Lett* 93:015501.
19. Funamori N, Sato T (2008) A cubic boron nitride gasket for diamond-anvil experiments. *Rev Sci Instrum* 79:053903.
20. Elliott S (1991) Origin of the first sharp diffraction peak in the structure factor of covalent glasses. *Phys Rev Lett* 67:711–714.
21. Zeidler A, et al. (2014) High-pressure transformation of SiO₂ glass from a tetrahedral to an octahedral network: A joint approach using neutron diffraction and molecular dynamics. *Phys Rev Lett* 113:135501.
22. Li N, Sakidja R, Aryal S, Ching Wy (2014) Densification of a continuous random network model of amorphous SiO₂ glass. *Phys Chem Chem Phys* 16:1500–1514.
23. Wu M, Liang Y, Jiang Jz, Tse JS (2012) Structure and properties of dense silica glass. *Sci Rep* 2:398.
24. Sato T, Funamori N, Yagi T (2013) Differential strain and residual anisotropy in silica glass. *J Appl Phys* 114:103509.
25. Prakapenka V, Shen G, Dubrovinsky L, Rivers M, Sutton S (2004) High pressure induced phase transformation of SiO₂ and GeO₂: difference and similarity. *J Phys Chem Sol* 65:1537–1545.
26. Kuwayama Y, Hirose K, Sata N, Ohishi Y (2005) The pyrite-type high-pressure form of silica. *Science* 309:923–925.
27. Dubrovinsky LS, et al. (2004) A class of new high-pressure silica polymorphs. *Phys Earth Planet Inter* 143:231–240.
28. Hemley RJ, et al. (1988) Pressure-induced amorphization of crystalline silica. *Nature* 334:52–54.
29. Oganov A, Gillan M, Price G (2005) Structural stability of silica at high pressures and temperatures. *Phys Rev B* 71:064104.
30. Tsuchiya T, Tsuchiya J (2011) Prediction of a hexagonal SiO₂ phase affecting stabilities of MgSiO₃ and CaSiO₃ at multimegabar pressures. *Proc Natl Acad Sci USA* 108:1252–1255.
31. Lyle MJ, Pickard CJ, Needs RJ (2015) Prediction of 10-fold coordinated TiO₂ and SiO₂ structures at multimegabar pressures. *Proc Natl Acad Sci USA* 112:6898–6901.
32. Dekura H, Tsuchiya T, Tsuchiya J (2011) First-principles prediction of post-pyrite phase transitions in germanium dioxide. *Phys Rev B* 83:134114.
33. Hoppe R (1979) Effective coordination numbers (ECoN) and mean fictive ionic radii (MEFIR). *Z Krist New Cryst Struct* 150:23–52.
34. Hales T (2005) A proof of the kepler conjecture. *Ann Math* 162:1065–1185.
35. Jaeger H, Nagel SR (1992) Physics of the granular state. *Science* 255:1523–1532.
36. Kantor I, et al. (2012) BX90: A new diamond anvil cell design for x-ray diffraction and optical measurements. *Rev Sci Instrum* 83:125102.
37. Fei Y, et al. (2007) Toward an internally consistent pressure scale. *Proc Natl Acad Sci USA* 104:9182–9186.
38. Prescher C, Prakapenka VB (2015) DIOPTAS: A program for reduction of two-dimensional x-ray diffraction data and data exploration. *High Press Res* 35:223–230.
39. Weck G, et al. (2013) Use of a multichannel collimator for structural investigation of low-Z dense liquids in a diamond anvil cell: Validation on fluid H₂ up to 5 GPa. *Rev Sci Instrum* 84:063901.
40. Prescher C (2017) Glassure: An API and GUI program for analyzing angular dispersive total X-ray diffraction data. *Zenodo*, 10.5281/zenodo.880836.
41. Kaplow R, Strong SL, Averbach BL (1965) Radial density functions for liquid mercury and lead. *Phys Rev* 138:A1336–A1345.
42. Lorch E (1969) Neutron diffraction by germania, silica and radiation-damaged silica glasses. *J Phys C Solid State Phys* 229:229–237.
43. Perdew JP, Burke K, Ernzerhof M (1996) Generalized gradient approximation made simple. *Phys Rev Lett* 77:3865–3868.
44. Goedecker S, Teter M, Hutter J (1996) Separable dual-space Gaussian pseudopotentials. *Phys Rev B* 54:1703–1710.
45. Marx D, Hutter J (2000) Ab-initio molecular dynamics: Theory and implementation. *Modern Methods and Algorithms of Quantum Chemistry*, NIC, ed Grotendorst J (Forschungszentrum Jülich, Jülich, Germany), 1st Ed, pp 301–449.
46. Nosé S, Klein ML (1983) Constant pressure molecular dynamics for molecular systems. *Mol Phys* 50:1055–1076.
47. Hoover WG (1985) Canonical dynamics: Equilibrium phase-space distributions. *Phys Rev A* 31:1695–1697.
48. Smith W, Forester TR (1996) DL.POLY.2.0: A general-purpose parallel molecular dynamics simulation package. *J Mol Graph* 14:136–141.
49. Takada A, Richet P, Catlow CRA, Price GD (2004) Molecular dynamics simulations of vitreous silica structures. *J Non Cryst Sol* 345–346:224–229.
50. Demiralp E, Çağın T, Goddard WA, III (1999) Morse stretch potential charge equilibrium force field for ceramics: Application to the quartz-stishovite phase transition and to silica glass. *Phys Rev Lett* 83:3749–3749.
51. Jülich Supercomputing Centre (2015) JUQUEEN: IBM blue Gene/Q supercomputer system at the Jülich supercomputing centre. *J Large Scale Res Facil JLSRF* 1:A1.